

Research Article

Multiwideband Bandpass Filter Based on Folded Quad Cross-Stub Stepped Impedance Resonator

Gunawan Wibisono ¹, Teguh Firmansyah,² Herudin Herudin,² Muh Wildan,³
Toto Supriyanto,⁴ Mudrik Alaydrus,⁵ and Febrizal Ujang¹

¹Department of Electrical Engineering, Faculty of Engineering, Universitas Indonesia, Kampus Baru UI, Depok 16424, Indonesia

²Department of Electrical Engineering, Faculty of Engineering, Universitas Sultan Ageng Tirtayasa, Cilegon, Banten 42435, Indonesia

³Department of Aviation Engineering, Indonesian Civil Aviation Institute, Tangerang, Banten 15820, Indonesia

⁴Department of Electrical Engineering, Politeknik Negeri Jakarta, Kampus Baru UI, Depok 16424, Indonesia

⁵Department of Electrical Engineering, Universitas Mercu Buana, Meruya, Jakarta 11650, Indonesia

Correspondence should be addressed to Gunawan Wibisono; gunawan@eng.ui.ac.id

Received 27 February 2020; Revised 9 May 2020; Accepted 30 June 2020; Published 24 July 2020

Academic Editor: Symeon Nikolaou

Copyright © 2020 Gunawan Wibisono et al. This is an open access article distributed under the Creative Commons Attribution License, which permits unrestricted use, distribution, and reproduction in any medium, provided the original work is properly cited.

A multiwideband bandpass filter (MW-BPF) using a quad cross-stub stepped impedance resonator (QC-SSIR) was simulated, fabricated, and measured. The proposed QC-SSIR is designed on a four-series arrangement of crossed open stub (COS) structures where each open stub is developed with a step impedance resonator (SIR) structure to generate a wide bandwidth. Compared to the COS resonator, the QC-SSIR has a wider fractional bandwidth and good transmission coefficients and is compact. ABCD matrix analysis is used to investigate the filter structure. Furthermore, the MW-BPF is designed on an FR4 microstrip substrate with $\epsilon_r = 4.4$, thickness $h = 1.6$ mm, and $\tan \delta = 0.0265$. The results show that the proposed MW-BPF using a QC-SSIR achieves transmission coefficients/fractional bandwidths of -0.60 dB/49.3%, -1.49 dB/18.7%, and -1.93 dB/13.9% at 0.81 GHz, 1.71 GHz, and 2.58 GHz, respectively. Furthermore, to reduce the filter size, a folded QC-SSIR (FQC-SSIR) structure was also proposed. The results show that the proposed MW-BPF using an FQC-SSIR achieves transmission coefficients/fractional bandwidths of -0.57 dB/49.6%, -1.21 dB/17.7%, and -1.76 dB/12.5% at 0.82 GHz, 1.80 GHz, and 2.62 GHz, respectively. The size of the proposed MW-BPF using an FQC-SSIR is reduced by up to 46% compared with the MW-BPF using a QC-SSIR. Finally, the performance of the simulated MW-BPF based on the QC-SSIR and FQC-SSIR was in good agreement with the measurement results.

1. Introduction

In recent years, a multiband transceiver has been required to improve efficiency and support the development of various types of wireless communication standards [1–3]. As a subsystem of a multiband transceiver, a multiband bandpass filter (MB-BPF) is an important and essential component to reduce noise and interference at several frequency bands simultaneously [4, 5]. Microstrip filters play a significant role in the multiband microwave filter design because of their advantages in terms of fabrication simplicity, miniaturization,

low loss, and low cost [6, 7]. Some attractive methods frequently used for the MB-BPF design include quarter-wavelength step impedance resonators (SIRs) [8], trisection SIRs [9–12], cascaded multiband resonators [13], loaded crossed resonators [14], stub-loaded resonators (SLRs) [15], trimode SLRs [16], stub-loaded quarter-wavelength resonators [17], stub-loaded and defected ground resonators (DGSs) [18, 19], and crossed open stubs (COSs) [20–22]. The most challenging part of an MB-BPF design is to allow several passbands simultaneously without sacrificing any design freedom or additional drawbacks such as complex geometry and

increasing size. Recently, some studies of an MB-BPF have been published in [8–22]. The results show a good electrical performance; however, the additional passbands would make the size of the BPF greater and the bandwidth narrower. Several studies on miniaturized microstrip BPFs have been reported such as BPFs using microstrip E-shaped bandpass filters [23], coupled slotted open stubs [24], and meander coupled lines [25].

The performance of an MB-BPF using a COS is proposed and evaluated in [21, 22], but these studies only resulted in a BPF with a narrow bandwidth. A COS method is an expansion method of SLRs, which is implemented by two open stubs with crossed positions; it is a good method due to its direct coupling. Therefore, the COS method has a good transmission coefficient (S_{21}) [21]. Moreover, the transmission zeros (TZs) can be easily controlled by adjusting the lengths and impedances of the COS.

Some research on multiwideband BPF (MW-BPF) was proposed in [24–26]. A very compact quintuple band BPF utilizing a multimode stub-loaded resonator (MSLR) was proposed in [26]. The proposed filter utilizes two coupled stub-loaded dual-mode resonators (SLDMRs) instead of three sets of resonators to achieve a compact triband BPF with good transmission coefficient and high selectivity [27]. A dual-wideband BPF and a triwideband BPF for 5G mobile communications are proposed in [28]. The dual-wideband BPF is achieved by two folded open-loop stepped impedance resonators (FOLSIRs), and then, by placing a pair of folded uniform impedance resonators (FUIRs) inside the dual-wideband BPF, a triwideband BPF is constituted with little influence on the physical size of the filter. The structure of the MW-BPF is complicated. A multiband BPF using a folded SIR was proposed in [4, 14, 29]; however, it generates a narrow bandwidth.

As novelty, compact multiband BPFs with a wide bandwidth and good transmission coefficient, a quad cross-stub stepped impedance resonator (QC-SSIR) was proposed. The QC-SSIRs are expanded COS structures. Typically, the COS structures are arranged serially depending on the number of bands to be produced, as shown in Figure 1(a). However, the bandwidth is still narrow. The combination of several COSs with the SIR structure called a crossed stub-SIR (CS-SIR) will be used to produce a wider bandwidth than the COS structure. This paper will propose three wideband BPFs using 4 CS-SIRs called quad-CS-SIRs (QC-SSIRs), as shown in Figure 1(b). Furthermore, to reduce the filter size, a folded QC-SSIR (FQC-SSIR) structure was proposed, as shown in Figure 1(c). As a result, the proposed multiband BPF exhibits not only a wide bandwidth, as shown in Figure 1(d), but also a compact size.

Furthermore, MW-BPFs using a QC-SSIR and FQC-SSIR were designed on an FR4 microstrip substrate with $\epsilon_r = 4.4$, thickness $h = 1.6$ mm, and loss tangent $\tan \delta = 0.0265$. The MW-BPF is simulated by using the

momentum simulation advanced system design (ADS). To validate the proposed method, the multiband BPF has been tested. The structure of this paper is as follows. Section 1 gives an overview of the proposed multiband BPF. Section 2 analyzes the structure of the COS, QC-SSIR, and FQC-SSIR. Section 3 focuses on the fabrication and measurement. Finally, Section 4 concludes this research.

2. Proposed COS, QC-SSIR, and FQC-SSIR Structure

This section analyzes the structure of a COS resonator, QC-SSIR, and FQC-SSIR based on ABCD matrix investigation.

2.1. Crossed Open Stub (COS) Structure. The COS resonator structure and the ABCD matrix structure for COS are shown in Figures 2(a) and 2(b), respectively. The input/output port is connected to 50Ω . In the COS topology, W_N and Z_N (for $N = S, 0, 1A, 2A, 3A$) represent the width and impedance of the resonator, respectively. L_N and θ_N (for $N = S, 0, 1A, 2A, 3A$) represent the physical length and electric length of the resonator, respectively. Furthermore, M_N (for $N = 1A, 2A, 3A, \text{COS}$) represents the ABCD matrix structure.

The ABCD matrix of the COS with the impedance of the transmission line, Z_N , and electrical length, θ_N , can be obtained as [20–22]

$$\begin{bmatrix} A_A & B_A \\ C_A & D_A \end{bmatrix} = M_{1A} M_{\cos(A)} M_{1A}, \quad (1)$$

with M_{1A} [30] as

$$M_{1A} = \begin{bmatrix} \cos \theta_{1A} & jZ_{1A} \sin \theta_{1A} \\ \frac{j \sin \theta_{1A}}{Z_{1A}} & \cos \theta_{1A} \end{bmatrix}, \quad (2)$$

and $M_{\cos(A)}$ can be calculated by parallel operation between Z_{2A} and Z_{3A} :

$$Z_{\cos(A)} = \frac{Z_{2A} Z_{3A} \cot \theta_{2A} \cos \theta_{3A}}{j(Z_{2A} \cot \theta_{2A} + Z_{3A} \cot \theta_{3A})}. \quad (3)$$

Because $M_{\cos(A)}$ has a position as open-stub circuited, the ABCD matrix of $M_{\cos(A)}$ becomes [31]

$$M_{\cos(A)} = \begin{bmatrix} 1 & 0 \\ Y_{\cos(A)} & 1 \end{bmatrix} = \begin{bmatrix} 1 & 0 \\ \frac{j(Z_{2A} \cot \theta_{2A} + Z_{3A} \cot \theta_{3A})}{Z_{2A} Z_{3A} \cot \theta_{2A} \cot \theta_{3A}} & 1 \end{bmatrix}. \quad (4)$$

Furthermore, the element matrix from equation (1) can be determined as follows:

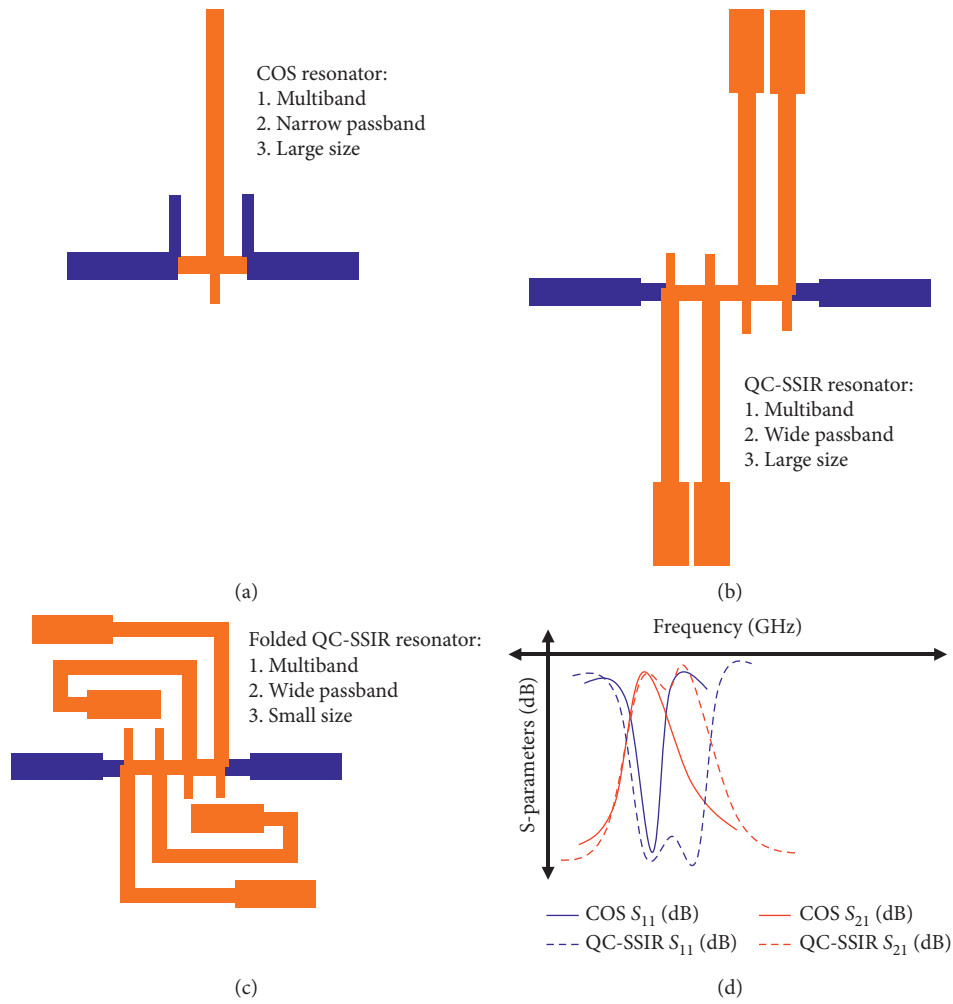


FIGURE 1: The resonator structure: (a) crossed open stub resonator, (b) quad cross-stub stepped impedance resonator (proposed), (c) folded quad cross-stub stepped impedance resonator (proposed), and (d) comparison of bandwidth of the COS and QC-SSIR structure.

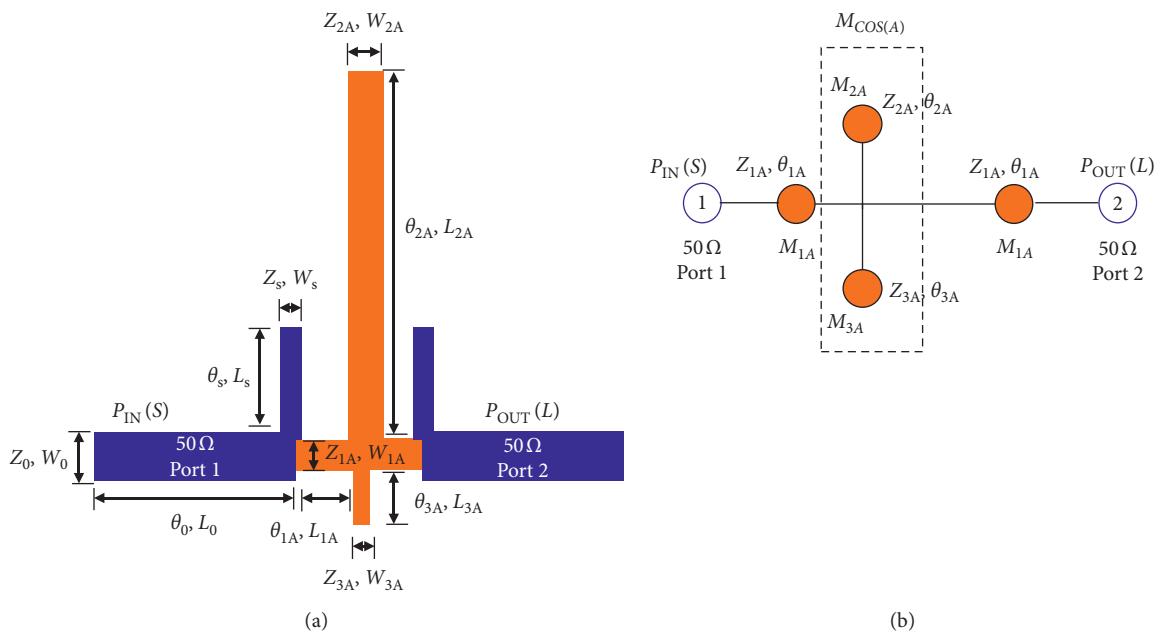


FIGURE 2: (a) The COS resonator structure and (b) the ABCD matrix structure for the COS resonator.

$$\begin{aligned}
A_A &= \cos^2 \theta_{1A} - \frac{Z_{1A} \sin \theta_{1A} \cos \theta_{1A} (Z_{2A} \cot \theta_{2A} + Z_{3A} \cot \theta_{3A})}{Z_{2A} Z_{3A} \cot \theta_{2A} \cot \theta_{3A}} - \sin^2 \theta_{1A}, \\
B_A &= jZ_{1A} \sin \theta_{1A} \left(\cos \theta_{1A} - \frac{Z_{1A} \sin \theta_{1A} (Z_{2A} \cot \theta_{2A} + Z_{3A} \cot \theta_{3A})}{Z_{2A} Z_{3A} \cot \theta_{2A} \cot \theta_{3A}} \right) + jZ_{1A} \sin \theta_{1A} \cos \theta_{1A}, \\
C_A &= \frac{j \sin \theta_{1A} \cos \theta_{1A}}{Z_{1A}} - \frac{\sin \theta_{1A} \cos \theta_{1A}}{Z_{1A}} \left(\frac{Z_{2A} \cot \theta_{2A} + Z_{3A} \cot \theta_{3A}}{Z_{2A} Z_{3A} \cot \theta_{2A} \cot \theta_{3A}} \right), \\
D_A &= -\sin^2 \theta_{1A} + j \cos^2 \theta_{1A} \left(\frac{Z_{2A} \cot \theta_{2A} + Z_{3A} \cot \theta_{3A}}{Z_{2A} Z_{3A} \cot \theta_{2A} \cot \theta_{3A}} \right).
\end{aligned} \tag{5}$$

To simplify the derivatives, we can set θ to $\lambda/4$ line or 90° so that the responses are determined by impedance only. Furthermore, to make equation (1) the closed-form equation, the same approach as proposed in [20–22] was used, which is that the ABCD matrix of the system is equivalent to the $\lambda/4$ line or set to the matching condition. Thus, the matrix ABCD can be written as

$$\begin{bmatrix} A & B \\ C & D \end{bmatrix} = \begin{bmatrix} \cos \theta_0 & jZ_0 \sin \theta_0 \\ \frac{j \sin \theta_0}{Z_0} & \cos \theta_0 \end{bmatrix} = \begin{bmatrix} 0 & jZ_0 \\ jY_0 & 0 \end{bmatrix}. \tag{6}$$

By solving equations (1) and (6), the transmission line impedance (Z_N) and electrical length (θ_N) of the COS resonator can be found. Finally, the relation of the ABCD matrix and the scattering parameters of S_{11} and S_{21} is determined by equations (7) and (8) [30], respectively:

$$S_{11} = \frac{A + BY_0 - CZ_0 - D}{A + BY_0 + CZ_0 + D}, \tag{7}$$

$$S_{21} = \frac{2}{A + BY_0 + CZ_0 + D}. \tag{8}$$

This conventional COS method only resulted in a narrow bandwidth and generated more than 3 resonance frequencies. To extend the bandwidth and reduce the number of resonance frequencies, this paper proposed a QC-SSIR to generate the MW-BPF. The proposed QC-SSIR is constructed by employing 2 identical SSIRs placed side by side, as shown in Figure 3(a).

2.2. Quad Cross-Stub Stepped Impedance Resonator (QC-SSIR) Structure. The proposed QC-SSIR structure and the ABCD matrix structure for the QC-SSIR are shown in Figures 3(a) and 3(b), respectively. The input/output port is connected to 50Ω . In the QC-SSIR topology, W_N and Z_N

(for $N = S, 0, 1B, 2B, 3B, 4B, 5B$) represent the width and impedance of the resonator, respectively. L_N and θ_N (for $N = S, 0, 1B, 2B, 3B, 4B, 5B$) represent the physical length and electric length of the resonator, respectively. Furthermore, M_N (for $N = 1B, 2B, 3B, 4B, 5B, \text{COS}$) represents the ABCD matrix structure.

The ABCD matrix of the QC-SSIR structure can be determined as follows:

$$\begin{bmatrix} A_B & B_B \\ C_B & D_B \end{bmatrix} = M_{1B} M_{\cos(B)} M_{5B} M_{\cos(B)} M_{5B} M_{\cos(B)} M_{5B} M_{\cos(B)} M_{1B}, \tag{9}$$

with

$$\begin{aligned}
M_{1B} &= \begin{bmatrix} \cos \theta_{1B} & jZ_{1B} \sin \theta_{1B} \\ \frac{j \sin \theta_{1B}}{Z_{1B}} & \cos \theta_{1B} \end{bmatrix}, \\
M_{5B} &= \begin{bmatrix} \cos \theta_{5B} & jZ_{5B} \sin \theta_{5B} \\ \frac{j \sin \theta_{5B}}{Z_{5B}} & \cos \theta_{5B} \end{bmatrix},
\end{aligned} \tag{10}$$

and $M_{\cos(B)}$ can be calculated by parallel operation between Z_{2B} and $Z_{SIR(B)}$:

$$\begin{aligned}
Z_{SIR(B)} &= \frac{j(Z_{3B} \tan \theta_{4B} + Z_{4B} \tan \theta_{3B})}{Z_{3B}(Z_{4B} - Z_{3B} \tan \theta_{3B} \tan \theta_{4B})}, \\
Z_{\cos(B)} &= \frac{Z_{2B} Z_{3B} \cot \theta_{2B} \tan \theta_{4B} + Z_{2B} Z_{4B} \cot \theta_{2B} \tan \theta_{3B}}{Z_{3B} Z_{4B} - Z_{3B}^2 \tan \theta_{3B} \tan \theta_{4B} - jZ_{2B} \cot \theta_{2B}}.
\end{aligned} \tag{11}$$

Because $M_{\cos(B)}$ has a position as open-stub circuited, the ABCD matrix of $M_{\cos(B)}$ becomes

$$M_{\cos(B)} = \begin{bmatrix} 1 & 0 \\ Y_{\cos(B)} & 1 \end{bmatrix} = \begin{bmatrix} 1 & 0 \\ \frac{Z_{3B} Z_{4B} - Z_{3B}^2 \tan \theta_{3B} \tan \theta_{4B} - jZ_{2B} \cot \theta_{2B}}{Z_{2B} Z_{3B} \cot \theta_{2B} \tan \theta_{4B} + Z_{2B} Z_{4B} \cot \theta_{2B} \tan \theta_{3B}} & 1 \end{bmatrix}. \tag{12}$$

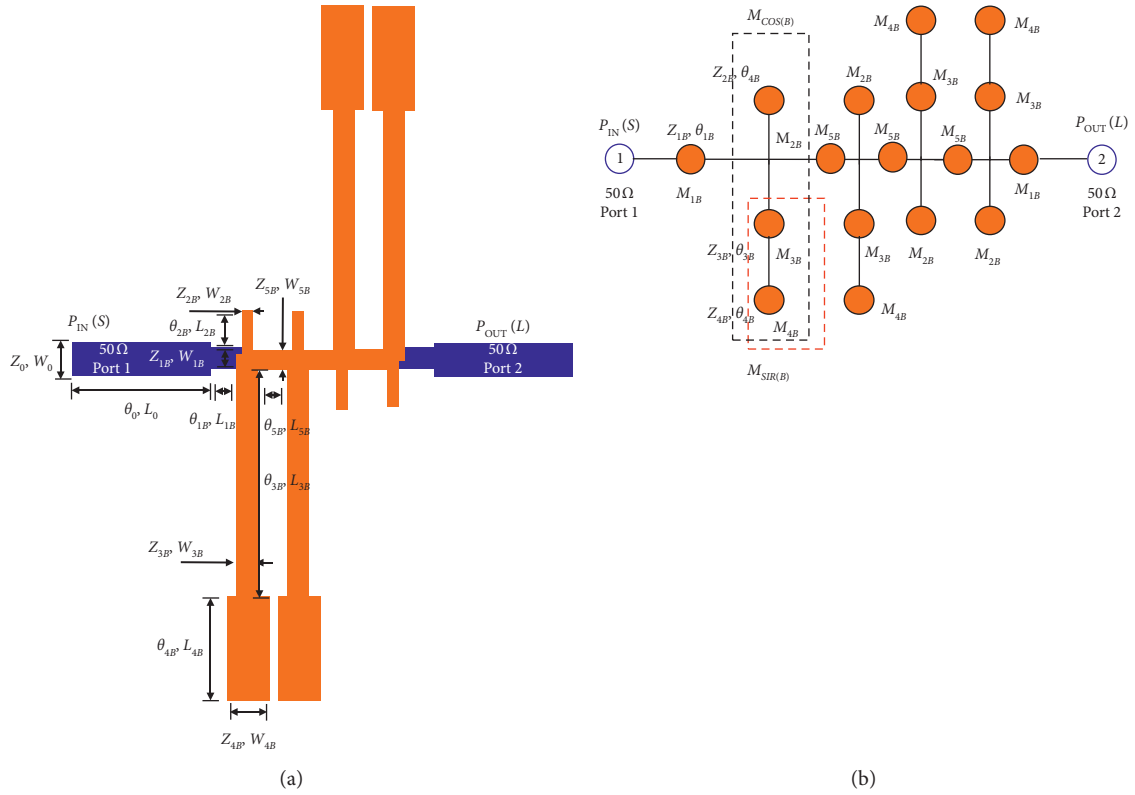


FIGURE 3: (a) QC-SSIR structure and (b) the ABCD matrix structure for the QC-SSIR.

To simplify the derivatives, we can set θ to $\lambda/4$ line or 90° so that the responses are determined by impedance only. The scattering parameters of S_{11} and S_{21} of the QC-SSIR structure can be obtained by solving equations (6)–(9).

Furthermore, Figures 4(a) and 4(b) show the transmission coefficients (S_{21}) and reflection coefficients (S_{11}) of the proposed MW-BPF with a QC-SSIR with varied L_{2B} values. The L_{2B} is varied from 0.5 mm to 4.5 mm by using ADS full-wave simulation software. The figure shows that the transmission coefficients at center frequencies of f_1, f_2 , and f_3 are stable; it also shows that the L_{2B} changes only slightly affect f_2 and f_3 . Moreover, the variation in L_{2B} was affected by the reflection coefficients (S_{11}) of f_2 and f_3 . Furthermore, the decrease in the reflection coefficient (S_{11}) of f_3 at $L_{2B} = 4.5$ mm is still lower than -10 dB.

Moreover, Figures 5(a) and 5(b) illustrate the transmission coefficients (S_{21}) and reflection coefficients (S_{11}) of the proposed MW-BPF using a QC-SSIR with varied L_{5B} values. The L_{5B} is varied from 3 mm to 15 mm. Figure 5(a) also shows the transmission zero frequencies, which were located at 1.2 GHz, 2.16 GHz, and 3.07 GHz. The result shows that the MW-BPF has three transmission zeros with good isolation. Figure 5(b) shows that the variation in L_{5B} was affected by the reflection coefficient (S_{11}) values, yet it has a slight effect on the frequency shift.

Figures 6(a)–6(c) show the reflection coefficients, transmission coefficients, and resonant frequencies of

the MW-BPF using a QC-SSIR with varied W_{4B}/W_{3B} values.

It can be seen from Figure 6(a) that the reflection coefficients (S_{11}) of frequencies f_1, f_2 , and f_3 can be tuned by modifying the values of W_{4B}/W_{3B} , whereas the reflection coefficients (S_{11}) of frequencies f_1, f_2 , and f_3 vary slightly. Meanwhile, Figure 6(b) shows the extracted transmission coefficients (S_{21}) with varied W_{4B}/W_{3B} values. It can be seen that the transmission coefficients (S_{21}) of frequencies f_1, f_2 , and f_3 are always increasing. Moreover, Figure 6(c) shows the resonant frequencies, where the frequency centers f_1, f_2 , and f_3 vary slightly. In general, the variation in W_{4B}/W_{3B} only affects the transmission coefficient values but does not affect the frequency shift. Furthermore, to reduce the filter size, a folded QC-SSIR (FQC-SSIR) structure was also proposed, as shown in Figure 7(a).

2.3. Folded Quad Cross-Stub Stepped Impedance Resonator (FQC-SSIR) Structure. The proposed folded quad cross-stub stepped impedance resonator (FQC-SSIR) structure and the ABCD matrix structure for the FQC-SSIR are shown in Figures 7(a) and 7(b), respectively. The input/output port is connected to $50\ \Omega$. In the FQC-SSIR topology, W_N and Z_N (for $N = S, 0, 1C, 2C, 3C, 4C, 5C$) represent the width and impedance of the resonator, respectively. L_N and θ_N (for $N = S, 0, 1C, 2C, 3C, 4C, 5C$) represent the physical length and electric length of the resonator, respectively.

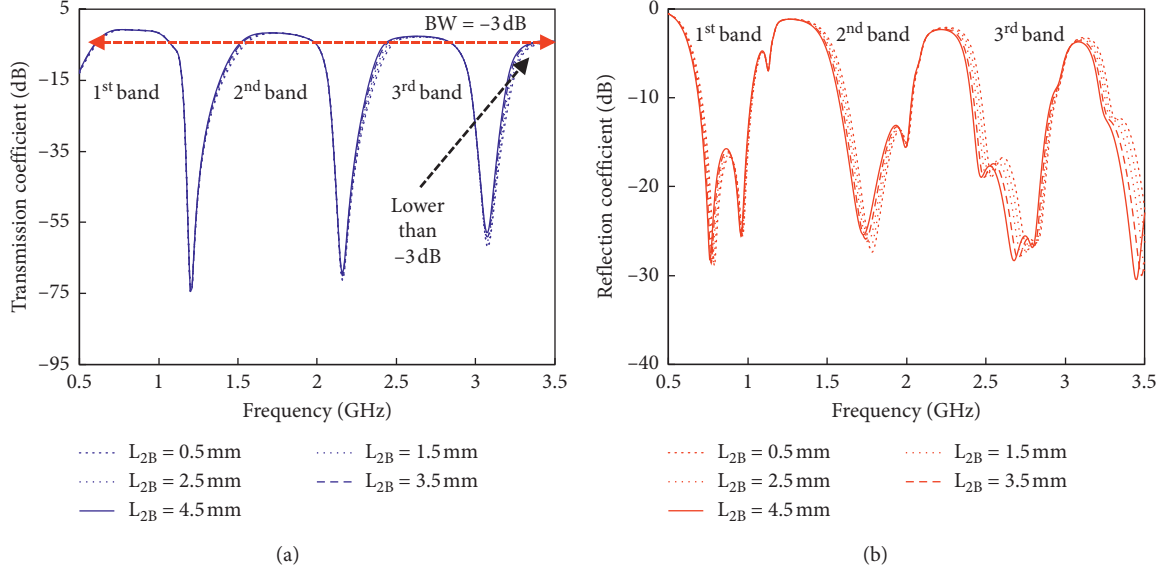


FIGURE 4: (a) The transmission coefficients (S_{21}) of the proposed MW-BPF using a QC-SSIR with varied L_{2B} values. (b) The reflection coefficients (S_{11}) of the proposed MW-BPF using a QC-SSIR with varied L_{2B} values.

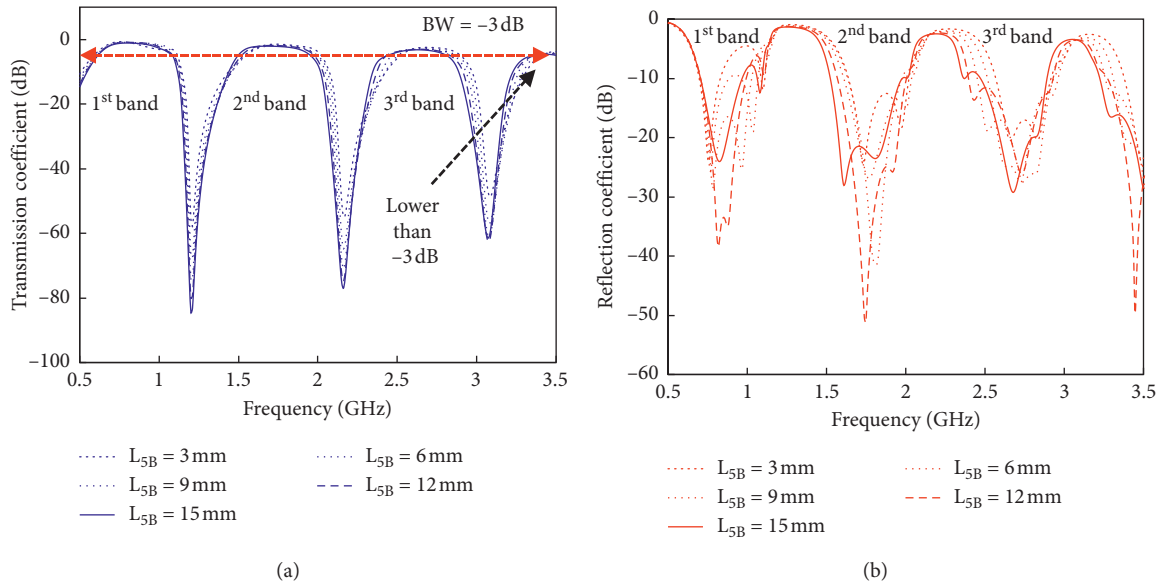


FIGURE 5: (a) The transmission coefficients (S_{21}) of the proposed MW-BPF using a QC-SSIR with varied L_{5B} values. (b) The reflection coefficients (S_{11}) of the proposed MW-BPF using a QC-SSIR with varied L_{5B} values.

Furthermore, M_N (for $N = 1C, 2C, 3C, 4C, 5C, COS$) represents the ABCD matrix structure.

The ABCD matrix of the folded QC-SSIR structure can be determined as follows:

$$\begin{bmatrix} A_C & B_C \\ C_C & D_C \end{bmatrix} = M_{1C} M_{\cos(C)} M_{5C} M_{\cos(C)} M_{5C} M_{\cos(C)} M_{5C} M_{\cos(C)} M_{1C}, \quad (13)$$

with

$$M_{1C} = \begin{bmatrix} \cos \theta_{1C} & jZ_{1C} \sin \theta_{1C} \\ \frac{j \sin \theta_{1C}}{Z_{1C}} & \cos \theta_{1C} \end{bmatrix}, \quad (14)$$

$$M_{5C} = \begin{bmatrix} \cos \theta_{5C} & jZ_{5C} \sin \theta_{5C} \\ \frac{j \sin \theta_{5C}}{Z_{5C}} & \cos \theta_{5C} \end{bmatrix}$$

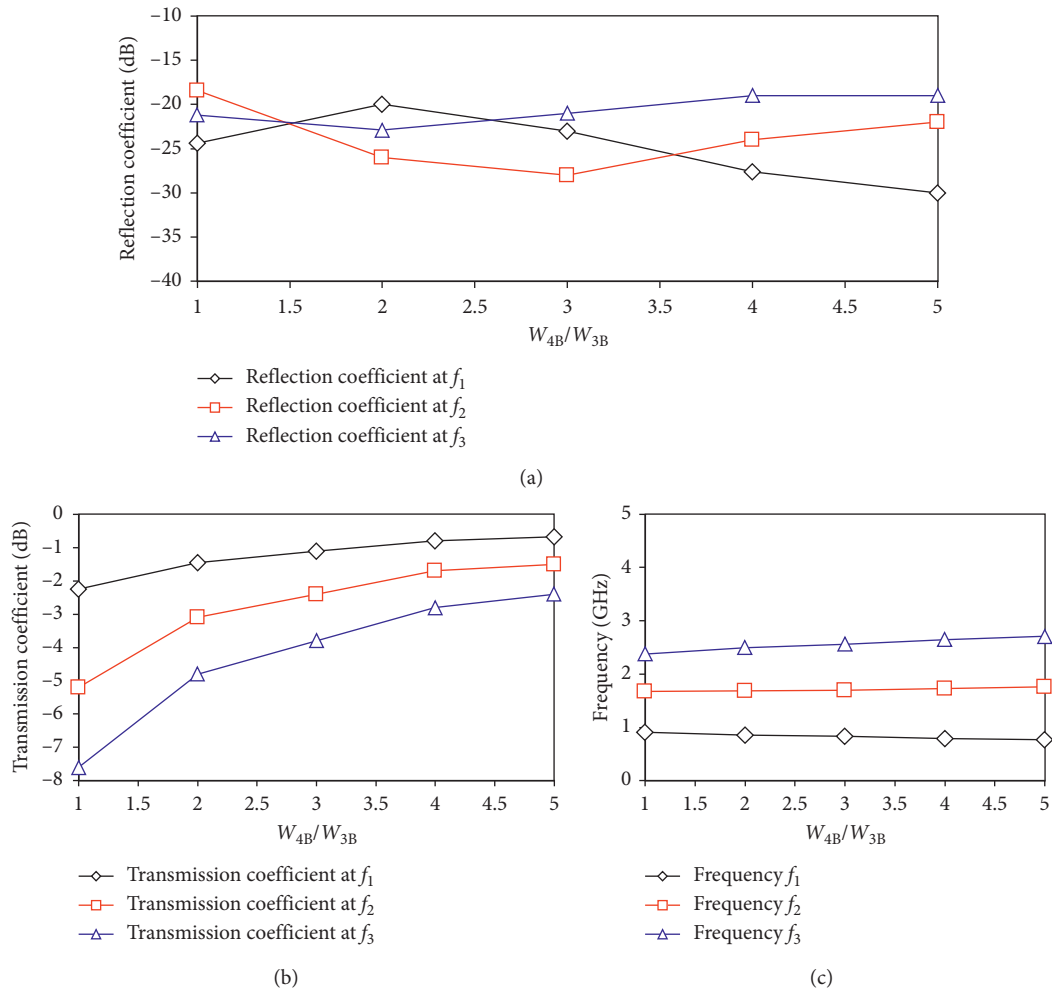


FIGURE 6: (a) The extracted reflection coefficients, (b) extracted transmission coefficients, and (c) extracted resonant frequencies of an MW-BPF using a QC-SSIR with varied W_{4B}/W_{3B} values.

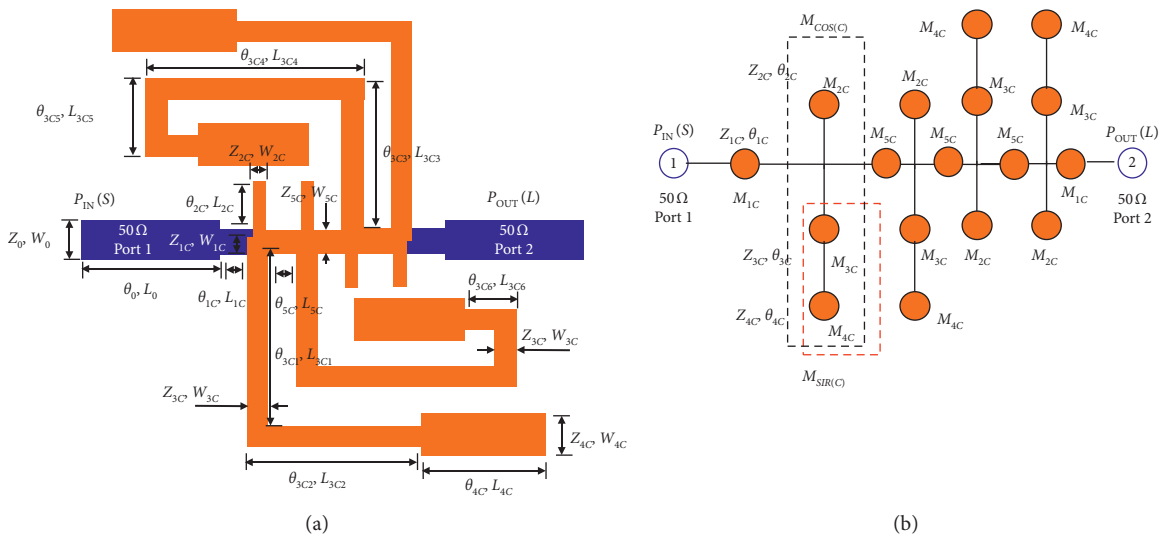


FIGURE 7: (a) FQC-SSIR structure and (b) the ABCD matrix structure for the FQC-SSIR.

and $M_{\cos(C)}$ can be calculated by parallel operation between Z_{2C} and $Z_{SIR(C)}$:

$$Z_{SIR(C)} = \frac{j(Z_{3C} \tan \theta_{4C} + Z_{4C} \tan \theta_{3C})}{Z_{3C}(Z_{4C} - Z_{3C} \tan \theta_{3C} \tan \theta_{4C})},$$

$$Z_{\cos(C)} = \frac{Z_{2C}Z_{3C} \cot \theta_{2C} \tan \theta_{4C} + Z_{2C}Z_{4C} \cot \theta_{2C} \tan \theta_{3C}}{Z_{3C}Z_{4C} - Z_{3C}^2 \tan \theta_{3C} \tan \theta_{4C} - jZ_{2C} \cot \theta_{2C}}. \quad (15)$$

$$M_{\cos(C)} = \begin{bmatrix} 1 & 0 \\ Y_{\cos(C)} & 1 \end{bmatrix} = \begin{bmatrix} 1 & 0 \\ \frac{Z_{3C}Z_{4C} - Z_{3C}^2 \tan \theta_{3C} \tan \theta_{4C} - jZ_{2C} \cot \theta_{2C}}{Z_{2C}Z_{3C} \cot \theta_{2C} \tan \theta_{4C} + Z_{2C}Z_{4C} \cot \theta_{2C} \tan \theta_{3C}} & 1 \end{bmatrix}. \quad (16)$$

To simplify the derivatives, we can set θ to $\lambda/4$ line or 90° so that the responses are determined by impedance only. The scattering parameters of S_{11} and S_{21} can be obtained by solving equations (6)–(8) and (13).

Furthermore, Figures 8(a) and 8(b) show the transmission coefficients (S_{21}) and reflection coefficients (S_{11}) of the proposed MW-BPF with a QC-SSIR with varied L_{2C} values. The L_{2C} is varied from 1.5 mm to 13.5 mm.

Figure 8(a) shows that the transmission coefficients at the center frequency of f_1 are stable. It also shows that the L_{2C} changes affect f_2 and f_3 . The 3rd bandwidth is degraded for the value $L_{2C} = 13.5$ mm. Furthermore, Figure 8(b) shows that the variation in L_{2B} was highly affected by the reflection coefficients (S_{11}) of f_2 and f_3 . It can be observed that by increasing the length of L_{2C} , the center frequencies of f_2 and f_3 gradually decrease. The reflection coefficient value (S_{11}) of f_3 is significantly decreased at $L_{2B} = 13$ mm. However, the values are still lower than -10 dB, with a relatively narrow bandwidth.

Furthermore, Figures 9(a) and 9(b) show the transmission coefficients (S_{21}) and reflection coefficients (S_{11}) of the proposed MW-BPF using an FQC-SSIR with varied L_{5C} values, respectively. It is clear from Figure 9(a) that the value of S_{21} is stable for f_1, f_2 , and f_3 . The graph indicates that the 4th passband does not appear because the value of S_{21} is lower than -3 dB. Moreover, the values of S_{11} for f_1, f_2 , and f_3 are significantly changed by varying L_{5C} . Figures 10(a)–10(c) show the reflection coefficients, transmission coefficients, and resonant frequencies of the MW-BPF using an FQC-SSIR with varied W_{4C}/W_{3C} values.

Figure 10(a) shows that the reflection coefficients (S_{11}) of frequency f_1 can be tuned by modified values of W_{4B}/W_{3B} , whereas the reflection coefficients (S_{11}) of frequencies f_2 and f_3 vary slightly. Additionally, Figure 10(b) shows the extracted transmission coefficients (S_{21}) with varied W_{4B}/W_{3B} values, and it can be seen that the transmission coefficients (S_{21}) of frequencies f_1, f_2 , and f_3 moderately increase. Moreover, Figure 10(c) shows the extracted resonant frequencies, where the frequency centers f_1, f_2 , and f_3 are mostly stable. In general, the variation in W_{4C}/W_{3C} only affects the

Because $M_{\cos(B)}$ has a position as open-stub circuited, the ABCD matrix of $M_{\cos(B)}$ becomes

reflection coefficient and marginally affects the transmission coefficient values or the frequency shift.

Furthermore, Figure 11 shows the transmission coefficients (S_{21}) and reflection coefficients (S_{11}) of the proposed MW-BPF using a folded QC-SSIR with a varied bend/corner structure. The performance of S_{21} and S_{11} by using the curve bend, square bend, and chamfer bend is compared. It is clearly seen that the chamfer bend generated good performance. However, the center frequencies of f_1, f_2 , and f_3 are moderately shifted.

3. Implementation of an MW-BPF Using a QC-SSIR and FQC-SSIR

To validate the proposed method, this section focuses on the fabrication and measurement. Figures 3(a) and 7(a) show the final schematic of the designed MW-BPF using a QC-SSIR and FQC-SSIR, respectively. The optimum dimensions of the MW-BPF structure using a QC-SSIR and FQC-SSIR were simulated by ADS. Furthermore, the proposed MW-BPF was fabricated on a microstrip with $\epsilon_r = 4.4$, $h = 1.6$ mm, and $\tan \delta = 0.0265$. As shown in Figure 3(a), the lengths of the transmission lines are $W_0 = 3.5$ mm, $W_{1B} = 1.0$ mm, $W_{2B} = 1.5$ mm, $W_{3B} = 2.5$ mm, $W_{4B} = 7.5$ mm, $W_{5B} = 2.5$ mm, $L_0 = 25$ mm, $L_{1B} = 1.0$ mm, $L_{2B} = 1.5$ mm, $L_{3B} = 77$ mm, $L_{4B} = 20$ mm, and $L_{5B} = 9.0$ mm. An FQC-SSIR structure is proposed to reduce the MW-BPF size, as shown in Figure 7(a). This miniaturization is performed by folding/rotating the length transmission line of the L_{3B} total length set to a constant of 77 mm. Moreover, the lengths of the transmission lines are $W_0 = 3.5$ mm, $W_{1C} = 1.0$ mm, $W_{2C} = 1.5$ mm, $W_{3C} = 2.5$ mm, $W_{4C} = 7.5$ mm, $W_{5C} = 2.5$ mm, $L_0 = 25$ mm, $L_{1C} = 1.0$ mm, $L_{2C} = 1.5$ mm, $L_{3C1} = 41$ mm, $L_{3C2} = 36$ mm, $L_{3C3} = 25$ mm, $L_{3C4} = 36$ mm, $L_{3C5} = 11$ mm, $L_{3C5} = 5.0$ mm, $L_{4C} = 20$ mm, and $L_{5C} = 9.0$ mm.

Figures 12(a) and 12(b) show photographs of the MW-BPF using a QC-SSIR and FQC-SSIR, respectively. Figure 12(a) shows that the MW-BPF using a QC-SSIR has a size of 97 mm \times 240 mm ($W_B \times L_B$). Meanwhile, the MW-BPF using an FQC-SSIR has a size of 97 mm \times 129 mm

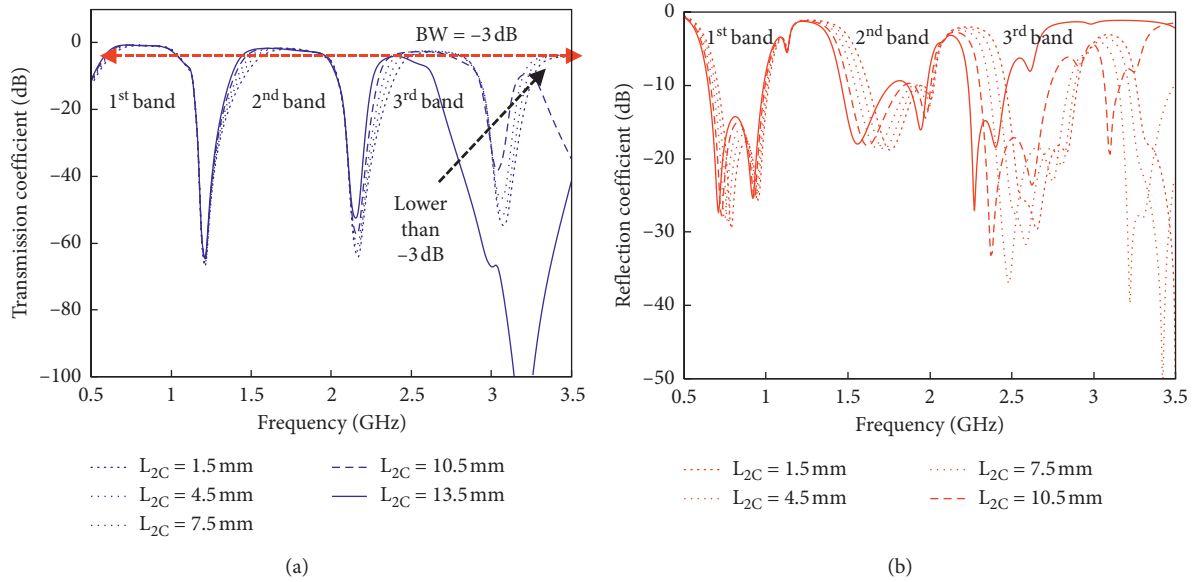


FIGURE 8: (a) Transmission coefficients (S_{21}) of the proposed MW-BPF using a folded QC-SSIR with varied L_{2C} values. (b) The reflection coefficients (S_{11}) of the proposed MW-BPF using a FQC-SSIR with varied L_{2C} values.

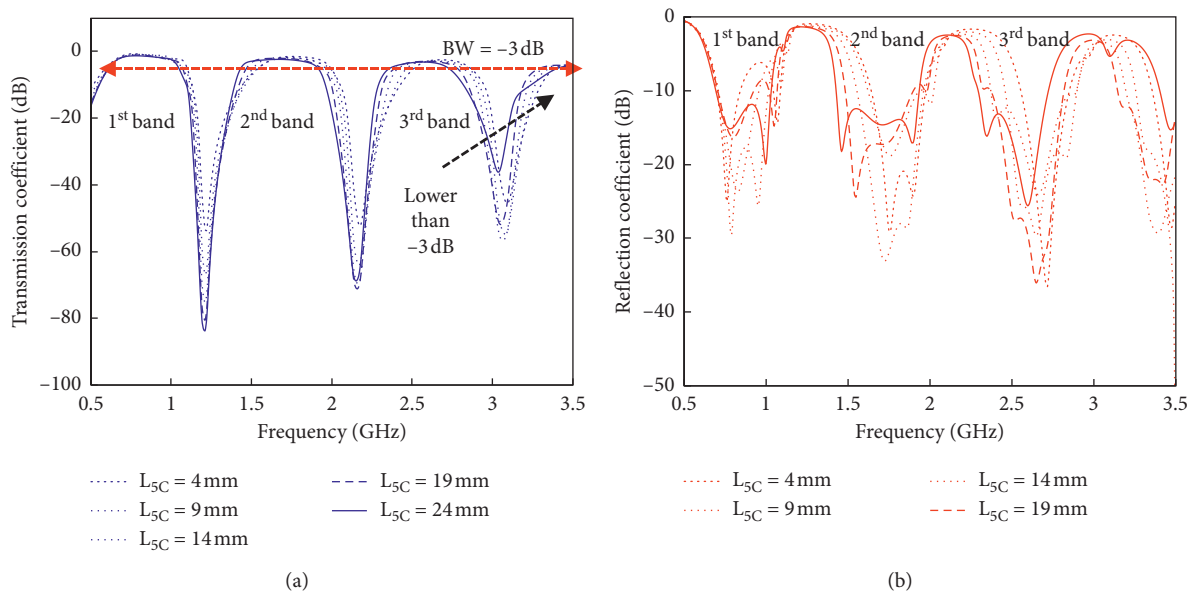


FIGURE 9: (a) Transmission coefficients (S_{21}) of the proposed MW-BPF using a folded QC-SSIR with varied L_{5C} values. (b) The reflection coefficients (S_{11}) of the proposed MW-BPF using an FQC-SSIR with varied L_{5C} values.

($W_C \times L_B$), as shown in Figure 12(b). Therefore, the size of the proposed MW-BPF with an FQC-SSIR is reduced by 46% compared to that of the MW-BPF with a QC-SSIR.

Figures 13(a) and 13(b) show comparisons between the simulated and measured results of the MW-BPFs using a QC-SSIR and FQC-SSIR in terms of the transmission coefficients (S_{21}) and reflection coefficients (S_{11}). We can see from Figure 13(a) that the value of transmission coefficients (S_{21}) has a ripple around a frequency of 1.8 GHz. However, this ripple does not occur at other frequencies, such as at the first band and the third band. We have investigated the cause of this ripple, and

the results show that imperfections in the cables and connectors cause the ripple. Overall, the performance of the proposed MW-BPF using an FQC-SSIR is slightly shifted within acceptable limits compared with the MW-BPF using a QC-SSIR. Both the MW-BPF using a QC-SSIR and that using an FQC-SSIR obtained good reflection coefficients lower than -10 dB.

The MW-BPF using a QC-SSIR achieves transmission coefficients/fractional bandwidths of 0.60 dB/49.3%, 1.49 dB/18.7%, and 1.93 dB/13.9% at 0.81 GHz, 1.71 GHz, and 2.58 GHz, respectively. Moreover, the MW-BPF using an FQC-SSIR achieves transmission coefficients/fractional

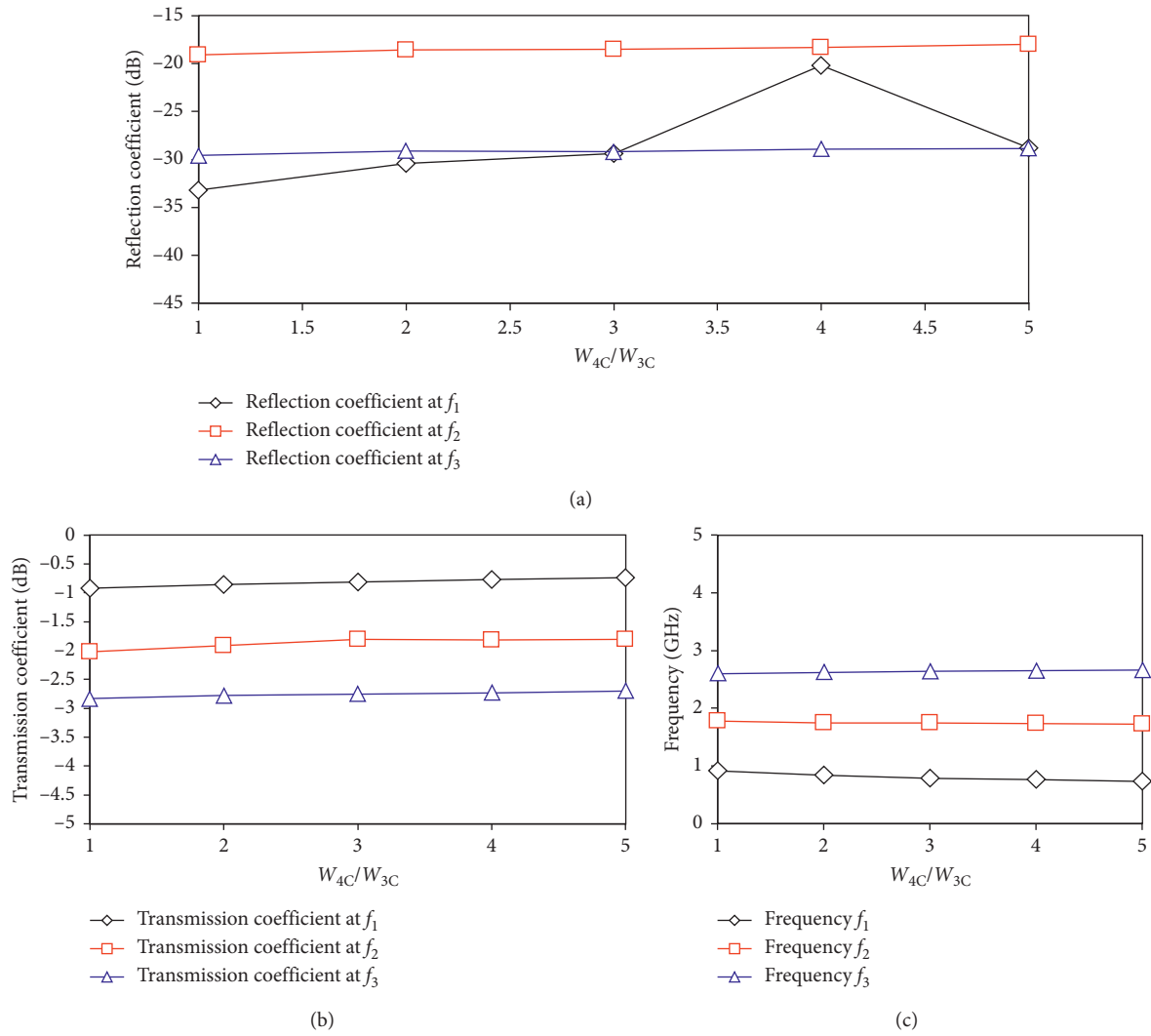


FIGURE 10: (a) The reflection coefficients, (b) transmission coefficients, and (c) resonant frequencies of the MW-BPF using an FQC-SSIR with varied W_{4C}/W_{3C} values.

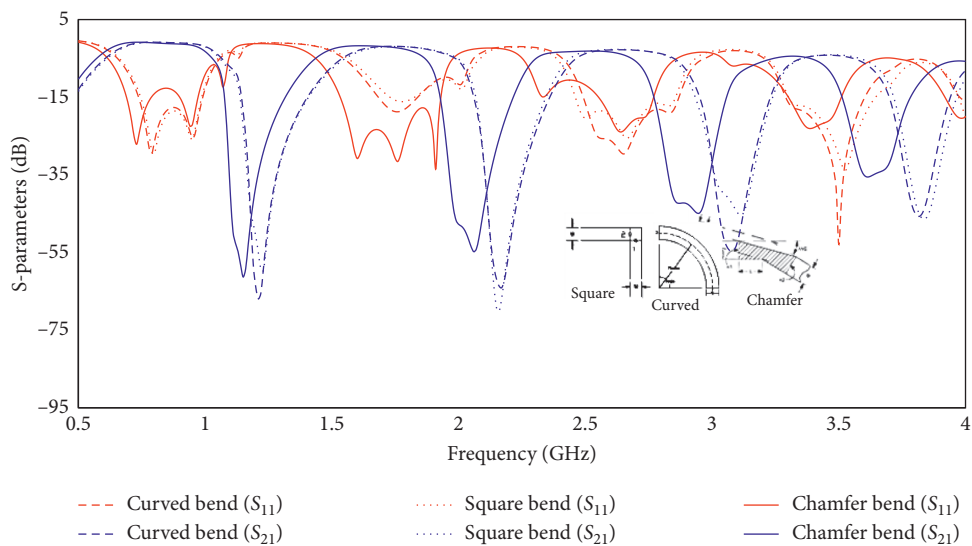


FIGURE 11: The transmission coefficients (S_{21}) and reflection coefficients (S_{11}) of the proposed MW-BPF using an FQC-SSIR with a varied bend/corner structure.

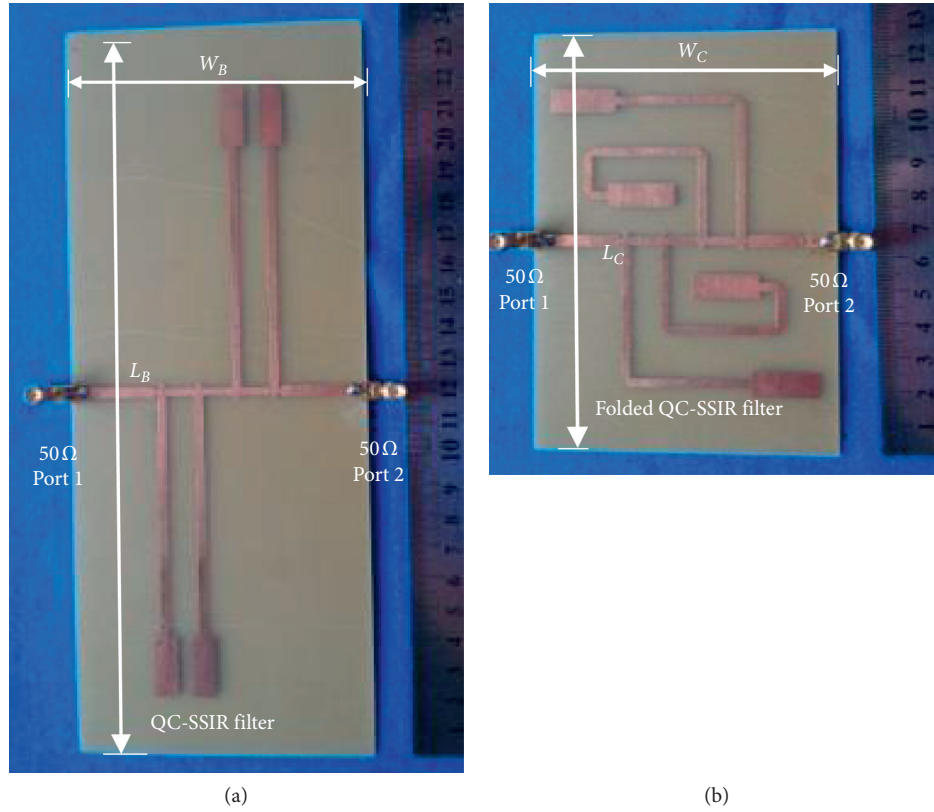


FIGURE 12: Photograph of MW-BPFs using a (a) QC-SSIR and (b) FQC-SSIR.

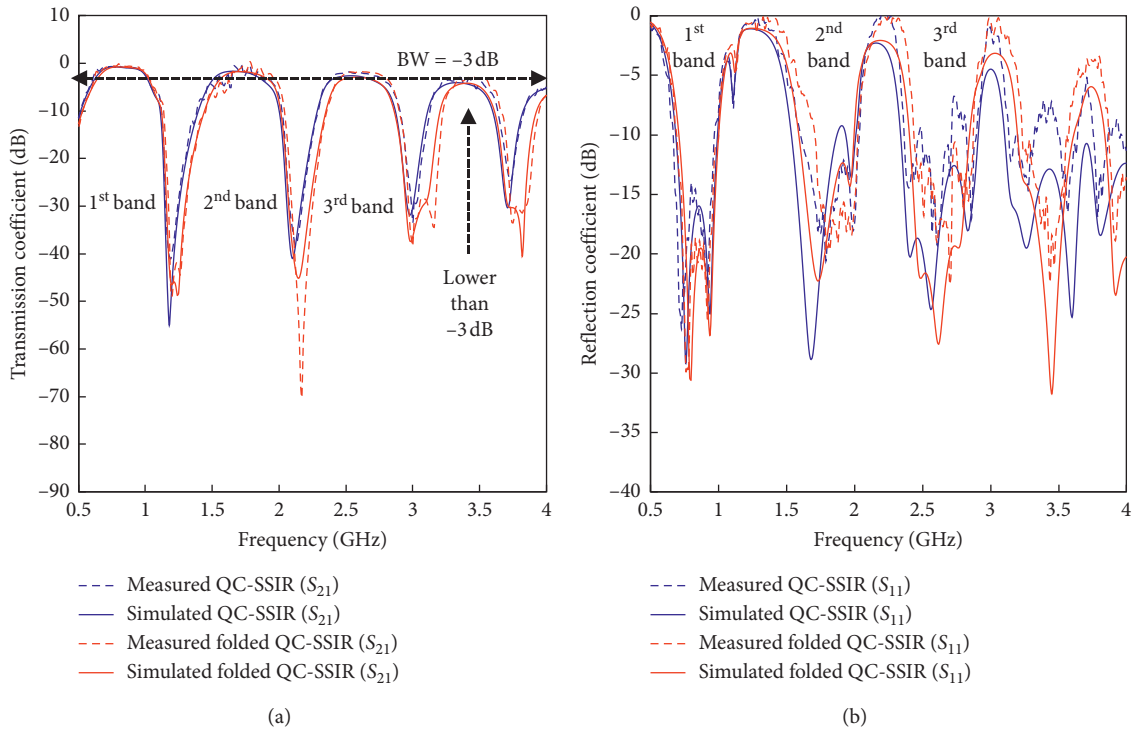


FIGURE 13: Comparison between the simulated and measured results of the MW-BPF using a QC-SSIR and FQC-SSIR in terms of the (a) transmission coefficients (S_{21}) and (b) reflection coefficients (S_{11}).

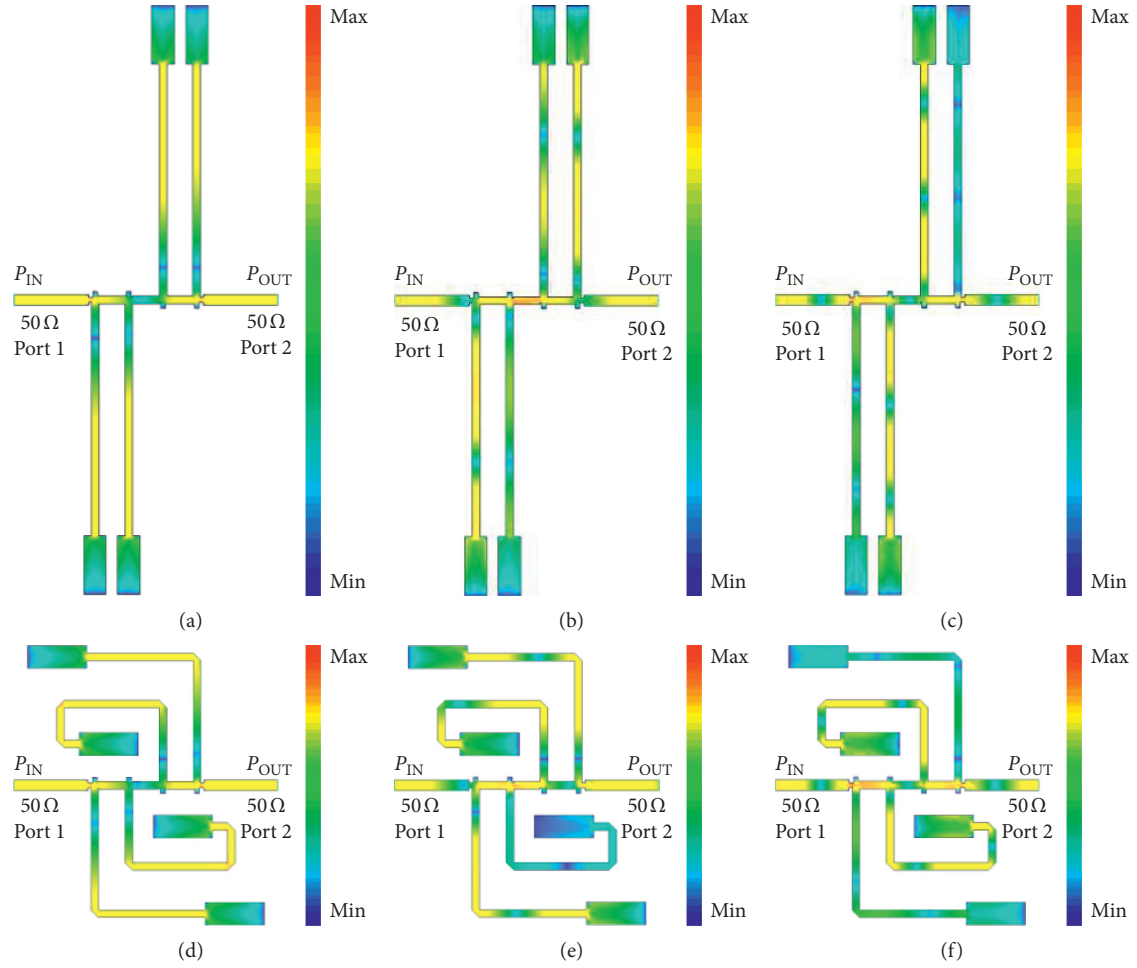


FIGURE 14: Surface current flow of a QC-SSIR at (a) f_1 , (b) f_2 , and (c) f_3 and an FQC-SSIR at (d) f_1 , (e) f_2 , and (f) f_3 .

TABLE 1: Summary of the proposed multiwideband BPF comparison.

Ref	Year	Method	Center frequency (GHz)	Transmission coefficients (dB)	-3 dB FBW (%)	Size (λ_g)
[8]	2006	Quarter-wavelength SIRs	1.57/2.45/5.25	-1.50/-1.34/-0.90	8.2/7.3/9.9	0.06×0.09
[10]	2007	Trisection SIRs	1.57/2.45/3.50	-1.95/-2.42/-2.00	7.0/4.2/9.0	0.12×0.09
[13]	2006	Cascaded multiband resonators	2.30/3.70/5.30	-2.50/-1.90/-2.90	3.8/6.8/5.0	0.28×0.68
[14]	2009	Loaded crossed resonator	2.40/3.50/5.20	-1.40/-1.50/-1.80	3.0/3.0/3.0	0.18×0.20
[16]	2010	Trimode stub-loaded resonators (SLRs)	2.45/3.56/5.90	-0.80/-1.60/-1.80	7.59/5.86/3.71	0.16×0.20
[17]	2011	Stub-loaded quarter-wavelength resonator	1.80/2.40/3.00	-0.30/-0.30/-0.20	9.4/12.5/6.4	0.23×0.30
[19]	2010	Stub-loaded and DGS resonator	2.45/3.50/5.25	-0.90/-1.70/-2.10	12.3/6.2/3.3	0.26×0.32
[22]	2010	Crossed open stubs	2.45/3.50/5.22	-0.80/-0.80/-0.80	15.1/13.4/7.6	0.20×0.30
[27]	2018	Two stub-loaded dual-mode resonators	1.57/2.40/3.45	-0.70/-1.14/-0.3	28.6/9.75/5.21	0.44×0.56
[28]	2020	Folded open-loop stepped impedance resonators	2.17/3.51/4.86	-0.46/-0.49/-1.30	12.4/11.4/13.3	0.22×0.22
[32]	2019	Common resonator feeding	3.0/6.0/9.0	-3.06/-2.71/-3.16	3.06/2.71/3.16	0.15×0.12
[33]	2019	Asymmetric shunted-line stepped impedance resonator	1.57/2.40/3.50	-0.10/-0.09/-0.11	5.2/4.25/2.7	0.076×0.26
[34]	2020	Multicoupled line stub-SIR	1.75/2.55/3.55	-0.55/-1.37/-1.37	21.2/4.7/8.4	0.32×0.12
This work	Figure 12(a)	Quad cross-stub stepped impedance resonator (QC-SSIR)	0.81/1.71/2.58	-0.60/-1.49/-1.93	49.3/18.7/13.9	0.27×0.66
	Figure 12(b)	Folded quad cross-stub stepped impedance resonator (FQC-SSIR)	0.82/1.80/2.62	-0.57/-1.21/-1.76	49.6/17.7/12.5	0.27×0.35

λ_g is the guided wavelength on the substrate at the center frequency of the first passband.

bandwidths of 0.57 dB/49.6%, 1.21 dB/17.7%, and 1.76 dB/12.5% at 0.82 GHz, 1.80 GHz, and 2.62 GHz, respectively.

Furthermore, Figures 14(a)–14(f) show the surface current flow of a QC-SSIR at f_1 , f_2 , and f_3 and a folded QC-SSIR at f_1 , f_2 , and f_3 . Different surface current flows are clearly observed at different frequencies. Moreover, Table 1 summarizes the comparison of the various proposed BPFs. Furthermore, this result indicated that the QC-SSIR can be utilized to produce a multiband BPF for multiband applications. Good agreement can be observed between the simulated and measured results, which demonstrates the validity of the design.

4. Conclusion

The MW-BPF was successfully designed and implemented using a QC-SSIR microstrip structure. The MW-BPF using a QC-SSIR achieves transmission coefficients/fractional bandwidths of 0.60 dB/49.3%, 1.49 dB/18.7%, and 1.93 dB/13.9% at 0.81 GHz, 1.71 GHz, and 2.58 GHz, respectively. The QC-SSIR has a size of $97 \text{ mm} \times 240 \text{ mm}$ ($W_B \times L_B$). To reduce the filter size, an FQC-SSIR was proposed. The MW-BPF using a FQC-SSIR achieves transmission coefficients/fractional bandwidths of 0.57 dB/49.6%, 1.21 dB/17.7%, and 1.76 dB/12.5% at 0.82 GHz, 1.80 GHz, and 2.62 GHz, respectively. The QC-SSIR has a size of $97 \text{ mm} \times 129 \text{ mm}$ ($W_C \times L_B$). Therefore, the size of the proposed MW-BPF with an FQC-SSIR is reduced by 46% compared with that of the MW-BPF with a QC-SSIR. In comparison with previous works, the QC-SSIR microstrip structure could produce wide bandwidth and good transmission coefficients. The simulated and measured results are in good agreement.

Data Availability

The datasets are available from the corresponding author on reasonable request.

Conflicts of Interest

The authors declare no conflicts of interest.

Acknowledgments

This research was funded by the Ministry of Research and Technology of the Republic of Indonesia, under the Doctoral Dissertation Research Grants. Contract no. NKB-416/UN2.RST/HKP.05.00/2020 and addendum no. NKB-3015/UN2.RST/HKP.05.00/2020.

References

- [1] R. Gomez-Garcia, L. Yang, and J.-M. Munoz-Ferreras, "Low-reflection signal-interference single- and multipassband filters with shunted lossy stubs," *IEEE Microwave and Wireless Components Letters*, vol. 30, no. 4, pp. 355–358, 2020.
- [2] X. Fan, Y. Tian, and Y. Zhao, "Optimal design of multiband microstrip antennas by self-renewing fitness estimation of particle swarm optimization algorithm," *International Journal of Antennas and Propagation*, vol. 2019, Article ID 2176518, pp. 1–9, 2019.
- [3] D. G. Rahn, M. S. Cavin, F. F. Dai et al., "A fully integrated multiband MIMO WLAN transceiver RFIC," *IEEE Journal of Solid-State Circuits*, vol. 40, no. 8, pp. 1629–1641, 2005.
- [4] T. Firmansyah, S. Praptodiyono, A. S. Pramudyo, C. Chairunissa, and M. Alaydrus, "Hepta-band bandpass filter based on folded cross-loaded stepped impedance resonator," *Electronics Letters*, vol. 53, no. 16, pp. 1119–1121, 2017.
- [5] T. Firmansyah, S. Praptodinoyo, R. Wiryadinata et al., "Dual-wideband band pass filter using folded cross-stub stepped impedance resonator," *Microwave and Optical Technology Letters*, vol. 59, no. 11, pp. 2929–2934, 2017.
- [6] H. Liu, J. Lei, J. Wan, Y. Wang, F. Yang, and S. Peng, "A miniaturized dual-mode bandpass filter using slot spurline technique," *International Journal of Antennas and Propagation*, vol. 2013, pp. 1–6, 2013.
- [7] Z. P. Wang, P. S. Hall, J. Kelly, and P. Gardner, "Microstrip tunable bandpass filter with the colinear resonators," *International Journal of Antennas and Propagation*, vol. 2013, pp. 1–5, 2013.
- [8] C.-H. Lee, C.-I. G. Hsu, and H.-K. Jhuang, "Design of a new tri-band microstrip BPF using combined quarter-wavelength SIRs," *IEEE Microwave and Wireless Components Letters*, vol. 16, no. 11, pp. 594–596, 2006.
- [9] C.-I. G. Hsu, C.-H. Lee, and Y.-H. Hsieh, "Tri-band bandpass filter with sharp passband skirts designed using tri-section SIRs," *IEEE Microwave and Wireless Components Letters*, vol. 18, no. 1, pp. 19–21, 2008.
- [10] Y.-C. Chen, Y.-H. Hsieh, C.-H. Lee, and C.-I. G. Hsu, "Tri-band microstrip BPF design using tri-section SIRs," in *Proceedings of the IEEE Antennas and Propagation International Symposium*, vol. 57, no. 1, p. 128, Honolulu, HI, USA, June 2007.
- [11] F. Song, B. Wei, L. Zhu, Y. Feng, R. Wang, and B. Cao, "A novel tri-band superconducting filter using embedded stub-loaded resonators," *IEEE Transactions on Applied Superconductivity*, vol. 26, no. 8, pp. 1–9, 2016.
- [12] Q.-X. Chu and X.-M. Lin, "Advanced triple-band bandpass filter using tri-section SIR," *Electronics Letters*, vol. 44, no. 4, p. 295, 2008.
- [13] C.-F. Chen, T.-Y. Huang, and R.-B. Wu, "Design of dual- and triple-passband filters using alternately cascaded multiband resonators," *IEEE Transactions on Microwave Theory and Techniques*, vol. 54, no. 9, pp. 3550–3558, 2006.
- [14] Q.-X. Chu, F.-C. Chen, Z.-H. Tu, and H. Wang, "A novel crossed resonator and its applications to bandpass filters," *IEEE Transactions on Microwave Theory and Techniques*, vol. 57, no. 7, pp. 1753–1759, 2009.
- [15] F.-C. Chen, Q.-X. Chu, and Z.-H. Tu, "Tri-band bandpass filter using stub loaded resonators," *Electronics Letters*, vol. 44, no. 12, p. 747, 2008.
- [16] Q. Yin, L.-S. Wu, L. Zhou, and W.-Y. Yin, "A tri-band filter using tri-mode stub-loaded resonators (SLRs)," in *Proceedings of the IEEE Electrical Design of Advanced Package & Systems Symposium EDAPS*, vol. 1, no. 3, pp. 4–7, Singapore, December 2010.
- [17] M. T. Doan, W. Che, K. Deng, and W. Feng, "Compact tri-band bandpass filter using stub-loaded resonator and quarter-wavelength resonator," in *Proceedings of the 2011 International Conference on Advanced Technologies for Communications (ATC 2011)*, vol. 2, pp. 308–311, Da Nang, Vietnam, August 2011.
- [18] Y. Rao, H. J. Qian, B. Yang, R. Gomez-Garcia, and X. Luo, "Dual-band bandpass filter and filtering power divider with ultra-wide upper stopband using hybrid microstrip/DGS dual-resonance cells," *IEEE Access*, vol. 8, pp. 23624–23637, 2020.

- [19] X. Lai, C.-H. Liang, H. Di, and B. Wu, "Design of tri-band filter based on stub loaded resonator and DGS resonator," *IEEE Microwave and Wireless Components Letters*, vol. 20, no. 5, pp. 265–267, 2010.
- [20] W. Feng, X. Duan, Y. Shi, X. Y. Zhou, and W. Che, "Dual-band branch-line couplers with short/open-ended stubs," *IEEE Transactions on Circuits and Systems II: Express Briefs*, vol. 7747, p. 1, 2020.
- [21] W. Feng, Q. Xue, and W. Che, "Compact dual-band bandpass filter based on stepped impedance resonators and T-shaped line," *Microwave and Optical Technology Letters*, vol. 52, no. 12, pp. 2721–2724, 2010.
- [22] W. Feng, W. Che, and Q. Xue, "Novel tri-band microstrip bandpass filter using crossed open stubs with different lengths," in *Proceedings of the 15th International Symposium on Antennas and Propagation (ISAP)*, vol. 1, pp. 4–7, Zhuhai, Macao, 2010.
- [23] R. T. Hammed, "Miniaturized dual-band bandpass filter using E-shape microstrip structure," *AEU - International Journal of Electronics and Communications*, vol. 69, no. 11, pp. 1667–1671, 2015.
- [24] A. Alburaihan, M. Aqeeli, and Z. Hu, "Miniaturized dual-wideband bandpass filter using coupled slotted open stubs," in *Proceedings of the IEEE MTT-S International Microwave Symposium (IMS)*, vol. 2016, pp. 1–3, San Francisco, CA, USA, May 2016.
- [25] V. K. Killamsetty and B. Mukherjee, "Miniaturised highly selective bandpass filter with very wide stopband using meander coupled lines," *Electronics Letters*, vol. 53, no. 13, pp. 889–890, 2017.
- [26] A. Sami and M. Rahman, "A very compact quintuple band bandpass filter using multimode stub loaded resonator," *Progress In Electromagnetics Research C*, vol. 93, pp. 211–222, 2019.
- [27] M. Rahman and J.-D. Park, "A compact tri-band bandpass filter using two stub-loaded dual mode resonators," *Progress In Electromagnetics Research M*, vol. 64, pp. 201–209, 2018.
- [28] Z. Hou, C. Liu, B. Zhang et al., "Dual-/Tri-wideband bandpass filter with high selectivity and adjustable passband for 5G mid-band mobile communications," *Electronics*, vol. 9, no. 2, p. 205, 2020.
- [29] G. Wibisono, T. Firmansyah, P. S. Priambodo, A. S. Tamsir, T. A. Kurniawan, and A. B. Fathoni, "Multiband bandpass filter (BPF) based on folded dual crossed open stubs," *International Journal of Technology*, vol. 5, no. 1, pp. 32–39, 2014.
- [30] J. S. Hong and M. J. Lancaster, *Microstrip Filters for RF/Microwave Applications*, Wiley, New York, NY, USA, 2001.
- [31] P. Jarry and J. N. Beneat, *Microwave Amplifier and Active Circuit Design Using the Real Frequency Technique*, John Wiley & Sons, New York, NY, USA, 2016.
- [32] C.-F. Chen, S.-F. Chang, K.-W. Zhou, J.-J. Li, and G.-Y. Wang, "Ultracompact microstrip dual- and triple-band bandpass filters with a common resonator feeding structure," *IET Microwaves, Antennas & Propagation*, vol. 13, no. 2, pp. 252–257, 2019.
- [33] H. Liu, Y. Wang, P. Wen, and S. Zheng, "Novel tri-band high-temperature superconducting bandpass filters using asymmetric shunted-line stepped-impedance resonator (SLSIR)," *IEEE Access*, vol. 7, pp. 32504–32509, 2019.
- [34] T. Firmansyah, M. Alaydrus, Y. Wahyu, E. T. Rahardjo, and G. Wibisono, "A highly independent multiband bandpass filter using a multi-coupled line stub-SIR with folding structure," *IEEE Access*, vol. 8, pp. 83009–83026, 2020.